




Effect of Scanning Strategy on Mechanical Properties of Ti-6Al-4V Alloy Manufactured by Laser Direct Energy Deposition

Marina O. Gushchina, Yulia O. Kuzminova , Egor A. Kudryavtsev, Konstantin D. Babkin, Valentina D. Andreeva, Stanislav A. Evlashin, and Evgeniy V. Zemlyakov

Submitted: 12 May 2021 / Revised: 23 September 2021 / Accepted: 8 October 2021

Direct energy deposition (DED) is an additive manufacturing method that allows repairing the broken parts and building the meter-scale samples. However, the printing of large parts is associated with huge residual stresses and martensite phase formation, which can change the geometry of final samples or initiate the crack. The last factor is especially important for titanium alloys. In this work, we investigated the effect of DED thermal history on the obtained structural and mechanical properties of Ti-6Al-4V using a thermocouple. It was demonstrated that printing with long pauses leads to α' phase formation, which embrittles the material. Continuous printing with small pauses between tracks leads to the formation of the dual $\alpha + \beta$ structure. The effect of the texture on the material properties is also discussed. As a result of the study, the specific DED process parameters allow the same mechanical characteristics for as-built titanium alloy and the alloy after heat treatment.

Keywords direct energy deposition, phase composition, Ti-6Al-4V, tensile properties, thermal history

1. Introduction

Ti-6Al-4V alloy is a widely used material in medicine, mechanical engineering, aircraft and space industries due to its low weight, high strength, and good corrosion resistance (Ref 1-3). However, printing the items using a strong material such as Ti-6Al-4V alloy leads to the material waste and high manufacturing cost. Additive manufacturing (AM) is a modern technique that allows building parts of complex geometry directly from the computer model. AM allows to reduce the material waste, production time, and cost of production for parts with complex geometry. Depending on the printing process parameters, AM materials demonstrate the same or higher strength characteristics than their analogs produced by conventional technologies (Ref 4-11). In practice, the strength properties of AM Ti-6Al-4V alloy are higher by 10% in the orthogonal to the build direction rather than in longitudinal, while the ductility characteristics are equally low, ~5% (Ref 4, 12, 13). Additionally, AM materials are associated with strong

residual stress in the material and the anisotropic behavior formed due to the high heat gradient between the top layers and the substrate. Heat treatment is usually required to improve the properties of AM Ti-6Al-4V alloy. It removes the residual stress and provides the dual $\alpha + \beta$ phase composition (Ref 14). But the reduction in ductility has a strong effect on the deposition of large parts. It can lead to crack formation and premature failure during the printing process. The phase composition has an essential effect on the Ti-6Al-4V properties consisting of the hexagonal close-packed (hcp) α phase and the body-centered cubic (bcc) β phase, but depending on the cooling rate, the formation of a hard and brittle martensite phase (α') is also possible. During the printing process, the cooling rate reaches the values of 10^4 - 10^6 K/s forming the α' phase (Ref 15-18). The cooling rate above 410 °C/s leads to the full martensite structure in Ti-6Al-4V alloy, while the rate of 1.5 °C/s provides the totally $\alpha + \beta$ composition (Ref 19). The higher fraction of the martensite phase increases the strength of AM Ti-6Al-4V alloy and significantly decreases the ductility (Ref 20). However, despite the high cooling rate at the AM process, it is possible to obtain the structure in AM Ti-6Al-4V alloy without α' phase by controlling the thermal history of the part. Simonelli et al. obtained a dual $\alpha + \beta$ structure by manipulating printing process parameters using the powder bed fusion technique (Ref 21). The scanning strategy changes allow to reduce the residual stress and influence the thermal history affecting the α' phase volume. It can be essential for printing critical parts of large items.

Many works are devoted to research of the effect of scanning strategy on the structure and residual stresses in materials produced by powder bed fusion (PBF) AM technology (Ref 22, 23). Strantz et al. showed the ability to reduce residual stresses in Laser PBF Ti-6Al-4V samples changing the scanning strategy (Ref 24). Stephenson et al. investigated the effect of scanning strategy on the grain size and preferred grain orientation for the Electron beam PBF samples (Ref 25). The researches of PBF technologies demonstrate the increase of

Marina O. Gushchina, Konstantin D. Babkin, and Evgeniy V. Zemlyakov, Advanced Digital Technologies World-Class Research Center, State Marine Technical University, Saint Petersburg, Russian Federation 190121; **Yulia O. Kuzminova and Stanislav A. Evlashin**, Center for Design, Manufacturing and Materials, Skolkovo Institute of Science and Technology, Bolshoy Boulevard 30, bld. 1, Moscow, Russian Federation 121205; **Egor A. Kudryavtsev**, Belgorod State University, Belgorod, Russian Federation 308015; **Valentina D. Andreeva**, Peter the Great St. Petersburg Polytechnic University, Saint Petersburg, Russian Federation 195251. Contact e-mail: yulia.kuzminova@skoltech.ru.

material quality by manipulating the scanning strategy. However, despite wide application of DED technology, there is a limited number of studies demonstrating the dependence between the build-up strategy and DED material properties. For example, the study shows the change in the maximum temperature for different areas of the 316L stainless steel sample depending on the build-up strategy (Ref 26). Li et al. decrease residual stress in the wire laser metal deposited Ti-6Al-4V samples by applying the bidirectional toolpath scanning instead of unidirectional scanning (Ref 27). However, this result cannot be repeated for big scale parts due to the difference in thermal histories (Ref 28).

Additional studies are required to understand the properties of AM Ti-6Al-4V alloy, especially the works considering such industrial technology as Direct Energy Deposition (DED). DED prints the parts layer-by-layer by adding the metal powder to a substrate and heating it with different heat sources, laser or electron beams (Ref 29). The advantages of that technique are the high speed of building, low requirements to the powder quality, and the possibility of printing the gradient materials. The application of AM technology to Ti-6Al-4V alloy is highly prospective, while the number of studies considering the properties of AM Ti-6Al-4V alloy is still limited for large-scale parts.

The current work shows the changes of phase compositions of Ti-6Al-4V produced by changing DED printing strategy. Building the part with the specific phase composition allows excluding the heat treatment process, which is undesirable in the manufacture of large parts. The effect of the thermal history on the mechanical properties and structure of DED Ti-6Al-4V alloy is evaluated. Additionally, the impact of heat treatment is demonstrated.

2. Methods and Materials

2.1 Material

Figure 1(a) and (b) demonstrate the scanning electron microscope (SEM) images of the Ti-6Al-4V powder at low and high magnifications, respectively. The powder was produced by JSC “Kompozit” (Russia). The shape of the particles is mostly spherical with a smooth surface. Table 1 shows the powder element composition. Figure 1(c) presents the particle size

distribution, where the particle size is in the range of 50-150 μm with the mean particle size of 95 μm .

2.2 Printing Process

The machine produced by Institute of Laser and Welding Technologies (SMTU, Russia) was applied in the study, Fig. 2(a). The printing process was carried out by DED technique where the feedstock Ti-6Al-4V powder was applied to the melt path and melted by a laser heat source (L). The parts with dimensions of $75 \times 15 \times 35 \text{ mm}^3$ were produced in horizontal direction (Fig. 2b). All parts were printed on the pure Ti substrate without preheating in an argon environment with O_2 concentration controlled below 0.2 wt.%. The full list of deposition parameters is summarized in Table 2. Figure 2(c) demonstrates the three schemes of scan strategies used to print the parts: unidirectional hatching with a raster strategy performed in orthogonal directions X with a dwell time of 15 seconds between bead lines (Type A), continuous longitudinal hatching with a raster strategy performed in orthogonal directions X (Type B), and continuous transverse hatching with a raster strategy performed in orthogonal directions Y (Type C). Type A process parameters imitate the printing of a massive item where the next bead line is applied in a notable time. Type B and C process parameters imitate the common conditions of printing the lab samples.

Three additional parts were built with the different scan strategies, temperature was controlled by a tungsten-rhenium thermocouple (Tungsten 95%/Rhenium 5%-Tungsten 80%/Rhenium 20%). The scheme of a thermocouple installation is presented in Fig. 2(d). The block for measuring and recording temperature is assembled on the base of the X20ATC402 (B&R) module with a maximum measurement error of 25 $^\circ\text{C}$. The temperature recording cycle was 20 ms, the total measurement time was 1 h. To simplify the thermocouple installation, another geometry of the parts was chosen with dimensions of $65 \times 15 \times 110 \text{ mm}^3$. To minimize the platform

Table 1 Chemical composition of the Ti-6Al-4V powder (wt.%)

Ti	Al	V	Fe	C	S	N	O
Bal.	5.975	4.259	0.062	0.012	0.010	0.011	0.142

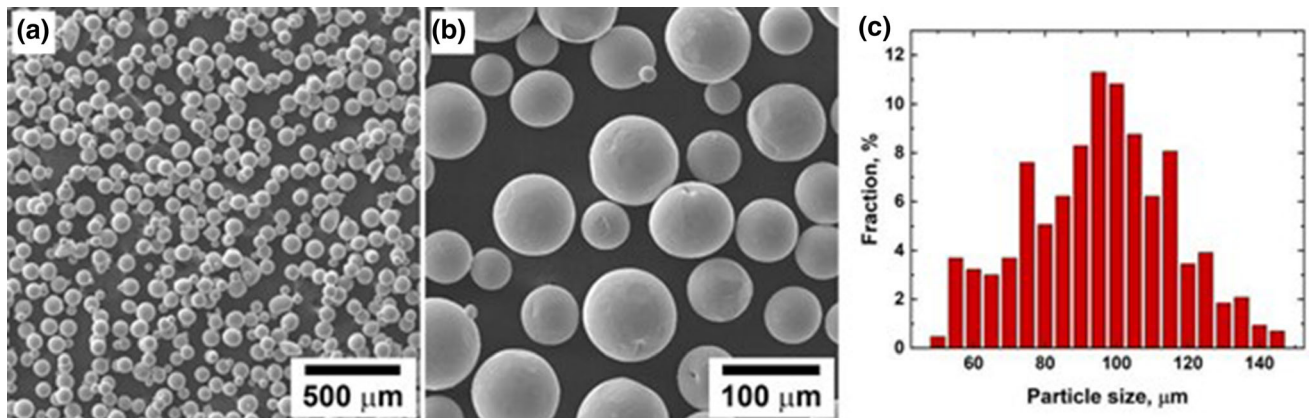


Fig. 1 SEM images of the Ti-6Al-4V powder at (a) low and (b) high magnifications; (c) the particle size distribution

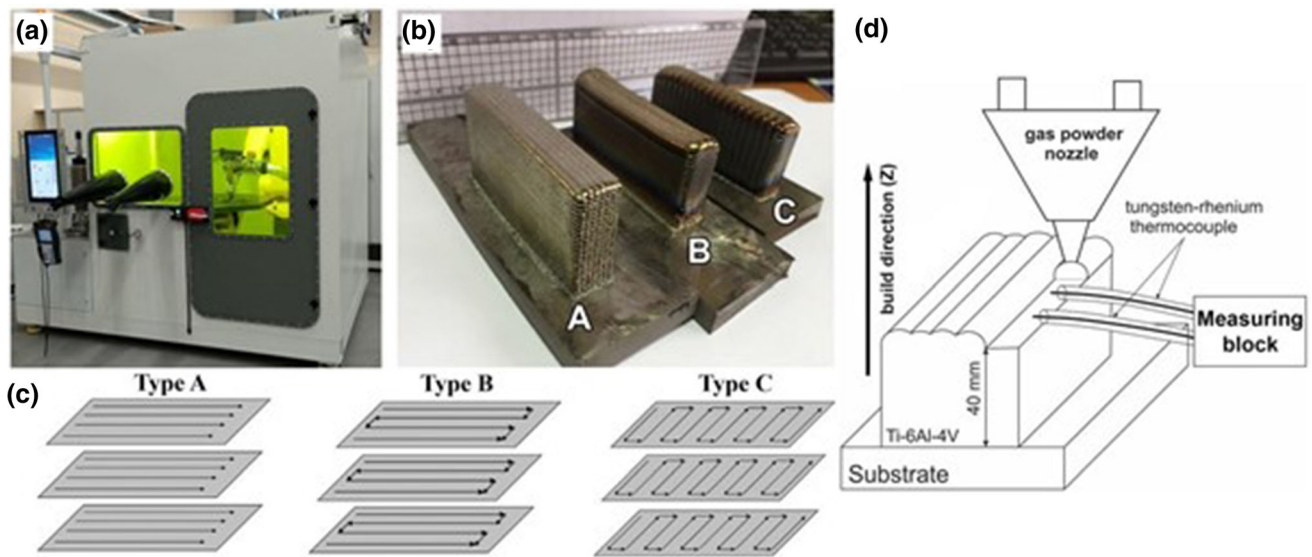


Fig. 2 (a) 3D printer used for the current work; (b) the as-built Ti-6Al-4V parts; (c) schemes of applied strategies; (d) schematic diagram of the thermal coupling setting

Table 2 The applied printing process parameters

Laser power, W	2200
Laser speed, mm/sec	20.0
Horizontal shift, mm	2.0
Layer thickness, mm	0.8
Laser spot diameter, mm	3.0
Argon consumption, l/min	25
Powder feed, g/min	11.8

effect, the thermocouple was placed in the middle of the part cross-section after the height reached the value of 40.0 mm.

2.3 Structural and Phase Analyses

The optical microscope DMI 5000 (Leica, Germany) with the “Axalit” software (Axalit, Russia) was used for microstructural analysis. The sample surfaces were polished with grit SiC papers up to 2500 grits with further polishing by an aluminum oxide suspension of 1 μm and final polishing with colloidal silica. As a final step, the etching procedure was conducted. The solution of 93 ml H_2O + 2 ml HF + 5 ml HNO_3 was applied to the polished sample surfaces for 40 seconds.

Scanning electron microscope Tescan Mira3 (TESCAN, Czech Republic) with console Oxford AZtec (Oxford Instruments NanoAnalysis, UK) was applied to analyze the fracture surface of tensile tested samples.

Electron backscatter diffraction (EBSD) analysis was conducted using a Nova NanoSEM microscope (FEI Company, Netherlands) equipped with an EBSD detector. The samples were polished up to 1 μm aluminum oxide suspension. EBSD maps were built with a step size of 0.3 μm .

Bruker Advance D8 diffractometer (Bruker, Germany) with $\text{CuK}\alpha$ radiation (wavelength = 1.5418 Å) was used to perform the XRD analysis. Detector is LynxEye linear position-sensitive detector (PSD) with a capture angle of 3.2 degrees 2θ . The cross-sectional surface of samples was polished with a grit SiC paper of 2500 grits and after etching measured in the 2θ range

of 34°–44° with a step size of 0.05 and an incremental time of 0.02.

2.4 Mechanical Tests

Half of the samples was cut from the as-built three parts with different scan strategies, and other samples were cut from the annealed parts. Vacuum heat treatment was conducted at a temperature of 900 °C for 2 h with cooling down to 400 °C in the furnace and further at air.

Tensile test was conducted at room temperature using the machine Zwick/Roell Z250 Allround series (Zwick/Roell, Germany). The standard cylindrical samples were cut from the printed parts according to geometry from the ASTM E8 with a gauge diameter of 6.0 mm and the gauge length of 24.0 mm. The sample displacement was recorded using an extensometer. During the test, the crosshead speed was 1.5 mm/min.

Microhardness measurements were performed with Microhardness tester FM-310 (Future Tech, Japan). The sample surface for testing was polished with 500 and 2500 grit SiC abrasive papers. At least 10 measurements per sample were conducted with a load of 300 g.

3. Results

3.1 Microstructure and Phase Composition

Figure 3 presents the three-dimensional optical images of as-built Ti-6Al-4V performed with different scan strategies. The optical analysis does not reveal the presence of pores for all three conditions. Figure 3(a) shows the cooled melting pool forming at a 15 s pause between the bead lines, which can be determined by optical methods after the etching procedure. Starting from the second layer, the Type A sample has a structure characterized by relatively smaller columnar grains with width of 400 μm and length of 1000 μm growing through the layer boundaries and orienting accordingly to the build direction. Type C sample has the largest columnar grains with

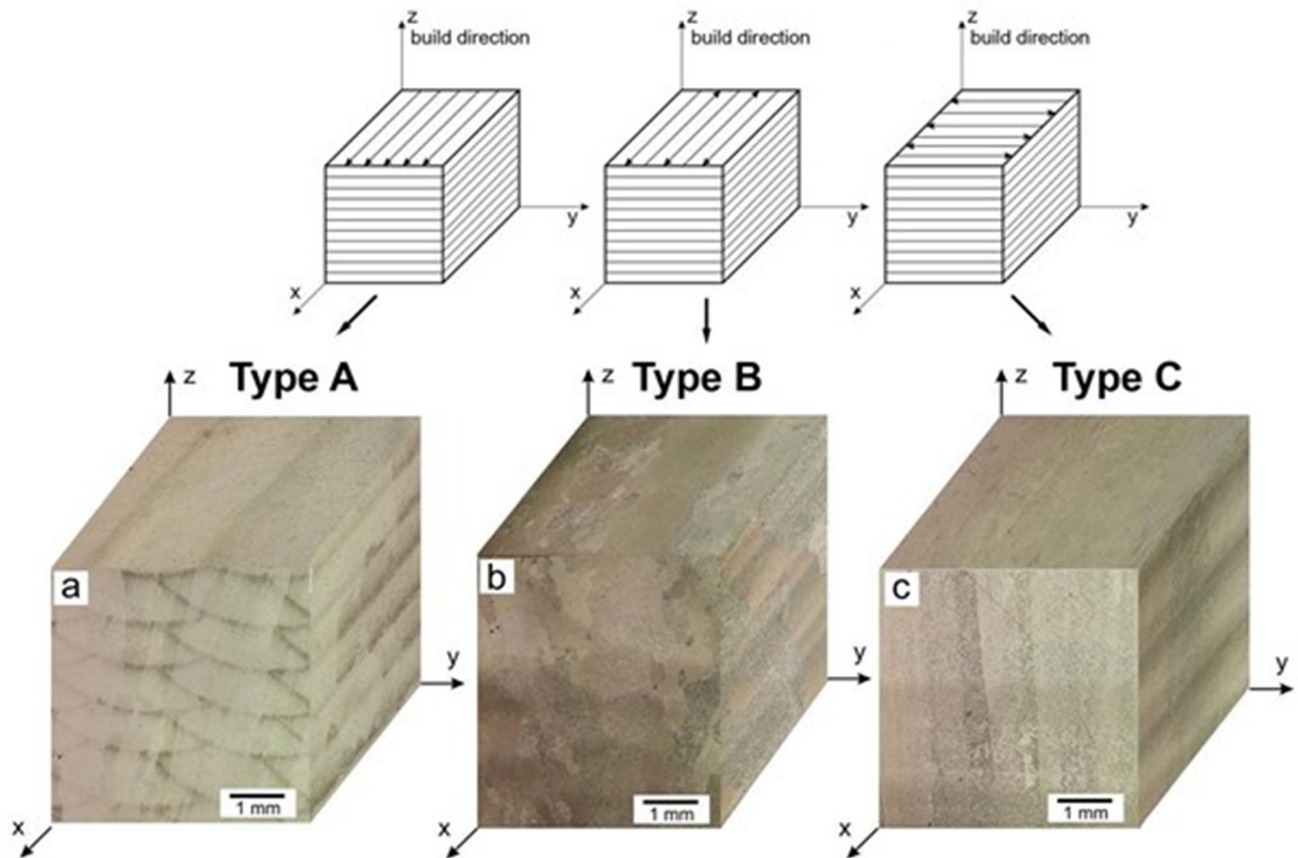


Fig. 3 Three-dimensional optical images of DED Ti-6Al-4V alloy produced with different scan strategies: (a) Type A, (b) Type B, and (c) Type C (Color figure online)

length of $7000\ \mu\text{m}$ and thickness of $750\ \mu\text{m}$ orientating along the build direction, Fig. 3(c). Type B sample demonstrates the intermediate structure between Types A and C characterized by equiaxed form with size of $500\text{-}1000\ \mu\text{m}$ (Fig. 3b).

Figure 4 shows the optical images of L-DED Ti-6Al-4V structures deposited with different scan strategies: (a, b) Type A, (c, d) Type B, and (e, f) Type C. Microstructure analysis shows the significance of the thermal history of the samples. Type A sample presenting a typical martensitic structure of Ti-6Al-4V alloy indicates the presence of metastable α' and α'' phases occurring at high cooling rates (more than $25\ ^\circ\text{C/s}$) from the β -region at a temperature above $1000\ ^\circ\text{C}$ (Ref 19). In practice, the α' and α'' phases are not considered separately due to their equally negative influence on the Ti-6Al-4V alloy mechanical properties. Type B sample demonstrates the equilibrium dual $\alpha + \beta$ phase composition, Fig. 4(c) and (d). Prior β -grains with the irregular forms and boundaries have the size in the range from 300 to $500\ \mu\text{m}$ (Fig. 4c). They consist of the α -lamellae with average length of $7\ \mu\text{m}$ and width of $1.5\ \mu\text{m}$ at different disordering states (Fig. 4d). This structure is typical for the as-casted Ti-6Al-4V alloy, but in L-DED conditions, it has a smaller α -lamella size. Type C structure (Fig. 4f) is similar to the Type B (Fig. 4d). It also demonstrates the dual lamellae composition with α -lamella sizes of $5\text{-}10\ \mu\text{m}$ length and $1\text{-}1.5\ \mu\text{m}$ width. However, the α -lamellae in the type C structure are mostly orientated at 45° to the build direction (Fig. 4e) in contrast to the lamellae in the B structure, which are orientated irregularly (Fig. 4c). Such structure is formed upon

significant overheating and a long standing time of the alloy above the polymorphic transformation temperature.

Figure 5 presents the EBSD maps according to the inverse pole figures and corresponded pole figures for L-DED Ti-6Al-4V alloy performed with (a) Type A, (b) Type B, and (c) Type C scan strategies. The analysis of grain size distribution reveals the high fraction of $1\ \mu\text{m}$ grains for Type A and Type C samples, 0.73 and 0.80 , respectively, while the Type B sample has a much lower $1\ \mu\text{m}$ -grain fraction of 0.48 . It indicates the relatively large α -lamellae size for the Type B sample, which can be seen in Fig. 5. The correlation between the preferable orientation in the material and scan strategy is observable. It should be noted that the α and α' phases are not considered separately due to the same Burgers orientation (Ref 30). Approximately $5\text{-}7$ orientations for α - and α' -lamellae are observed inside the β prior grains. Type A and Type B samples have the similar orientation of $\langle 0001 \rangle$ in the X-Y plane, in contrast to the Type C sample without preferable orientations. It can be explained by the higher effect of the part walls to the heat flow direction for Type C scan strategy due to another direction of hatch lines.

Figure 6 presents the structure of Ti-6Al-4V alloy performed with different scan strategies after annealing at $900\ ^\circ\text{C}$ for $2\ \text{h}$. Heat treatment forms the equilibrium $\alpha + \beta$ structure with α -lamella in the range of $10\text{-}20\ \mu\text{m}$ and width in the range of $1.5\text{-}2.5\ \mu\text{m}$ for all three conditions, Fig. 6(a), (b), (c).

Figure 7 demonstrates the XRD profiles for the three as-built samples printed with different scan strategies and the Type A sample after heat treatment. It reflects the contrast of the Type A

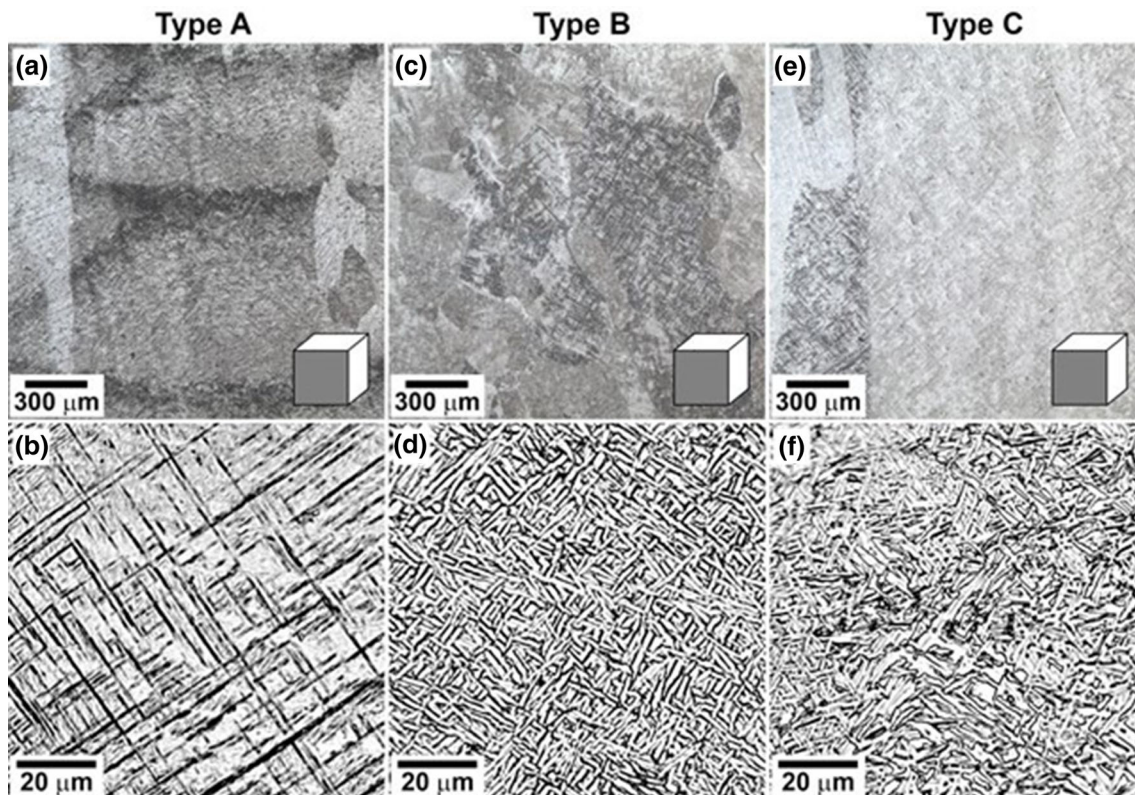


Fig. 4 Optical images of DED Ti-6Al-4V alloy (cross-sections parallel to the build direction)

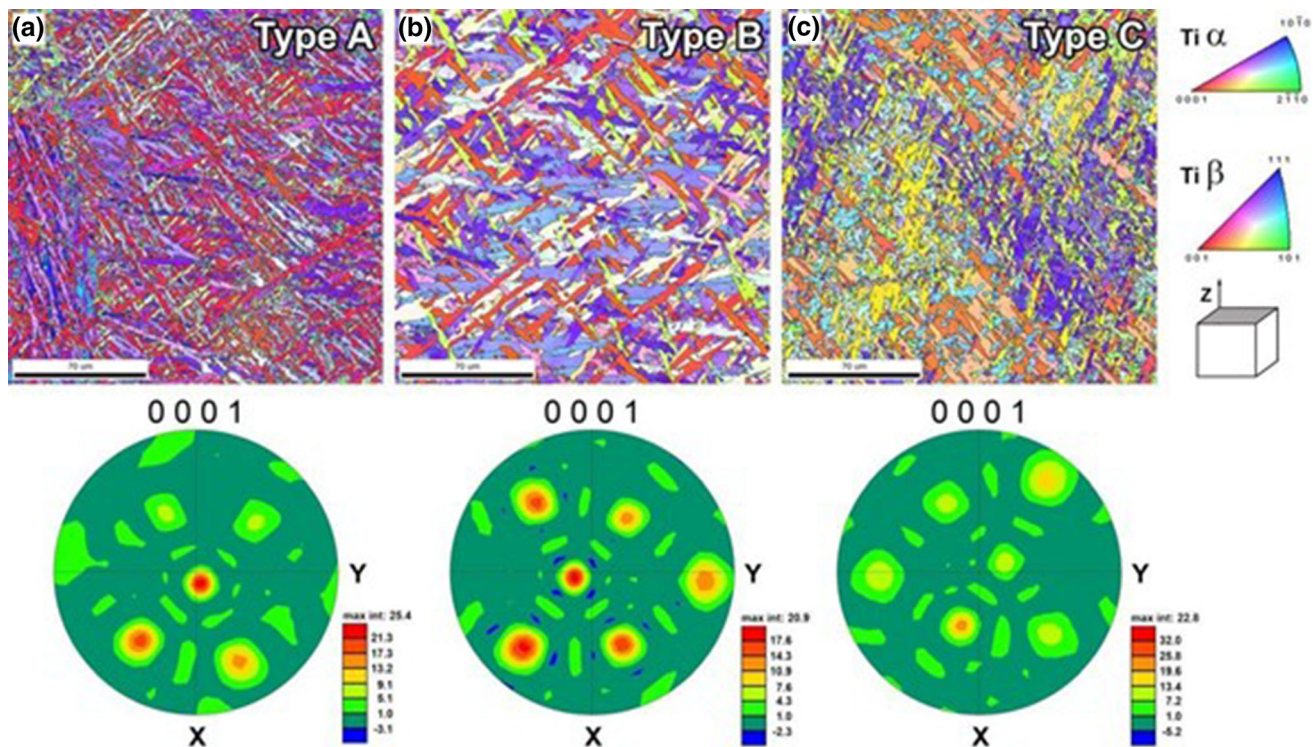


Fig. 5 EBSD orientation maps of DED Ti-6Al-4V alloy performed with (a) Type A, (b) Type B, and (c) Type C scan strategies and corresponded pole figures (front view) (Color figure online)

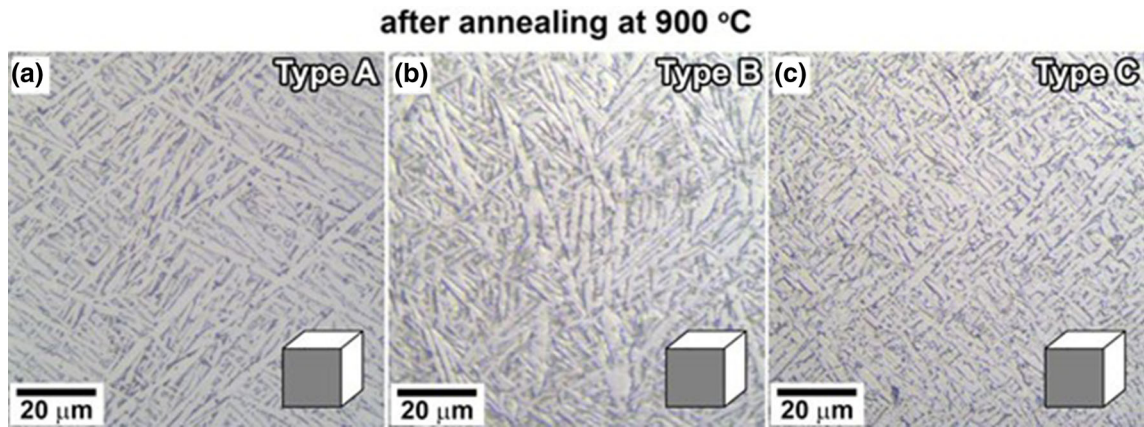


Fig. 6 Optical images of DED Ti-6Al-4V alloy performed with (a) Type A, (b) Type B, and (c) Type C scan strategies after annealing at 900 °C for 2 h (cross-sections parallel to the build direction)

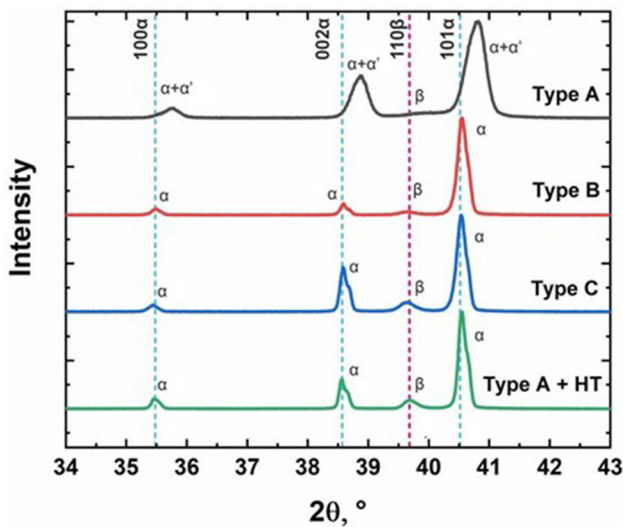


Fig. 7 XRD patterns of DED Ti-6Al-4V alloy obtained with Type A (gray), Type B (red), and Type C (blue) scan strategies and XRD pattern of Type A sample after heat treatment (HT) (green) from the top surface (Color figure online)

sample with dwell time of 15 seconds from other samples with continuous hatching. Shape of the peaks changes relative to a uniform distribution indicating the superimpose of reflections from similar hcp lattice of equilibrium α phase and nonequilibrium α' phase. The shifting of the peaks also reveals the presence of the martensite phase changing the lattice parameters. Because of higher solubility of Al and V in α' -Ti during fast cooling the lattice parameters of α' -Ti become lower which leads to shifting of diffraction peaks to higher angles for Type A where cooling rate is higher (Ref 31). Both XRD profiles for Types B and C samples correspond to the dual $\alpha + \beta$ composition. However, the Type C sample reveals the similar XRD pattern as for the annealed Type A sample presenting the fully $\alpha + \beta$ composition. At the same time, the XRD pattern of Type B has the relatively weaker intensity of β phase peak. After heat treatment, all samples present the same XRD profiles.

Figure 8 represents the thermal analyses obtained from the thermocouple during the printing of A, B, and C type samples. The size and shape of the thermal peaks significantly vary

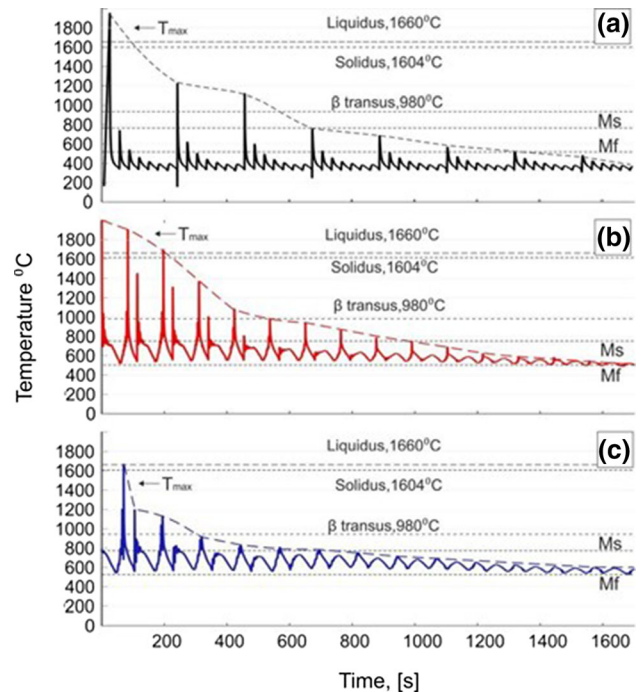


Fig. 8 The thermal cycles of DED Ti-6Al-4V alloy measured for 40 layers for (a) Type A, (b) Type B, and (c) Type C scan strategies. Ms and Mf dotted lines present the temperatures of the beginning and ending of martensite formation, respectively

depending on scan strategy choice. For Type A thermal curve, the cooling from the high temperature of above 950 °C to a temperature below 400 °C is typical (Fig. 8a). Such thermal behavior allows the diffusionless transformation of the β structure to a completely α/α' structure, Fig. 8(a). Type B and Type C curves are characterized by the relatively slow cooling rate to the T_{min} of 500-600 °C, Fig. 8(b) and (c), respectively. The annealing of the material at a temperature range of 550-800 °C provides the martensite decomposition. It agrees with the XRD analysis result revealing mostly $\alpha + \beta$ composition for Type B and Type C samples. Despite the similar shape of the temperature peaks for Type B and Type C curves, the layers in Type C are heated up to 8 cycles to temperatures above 950 °C,

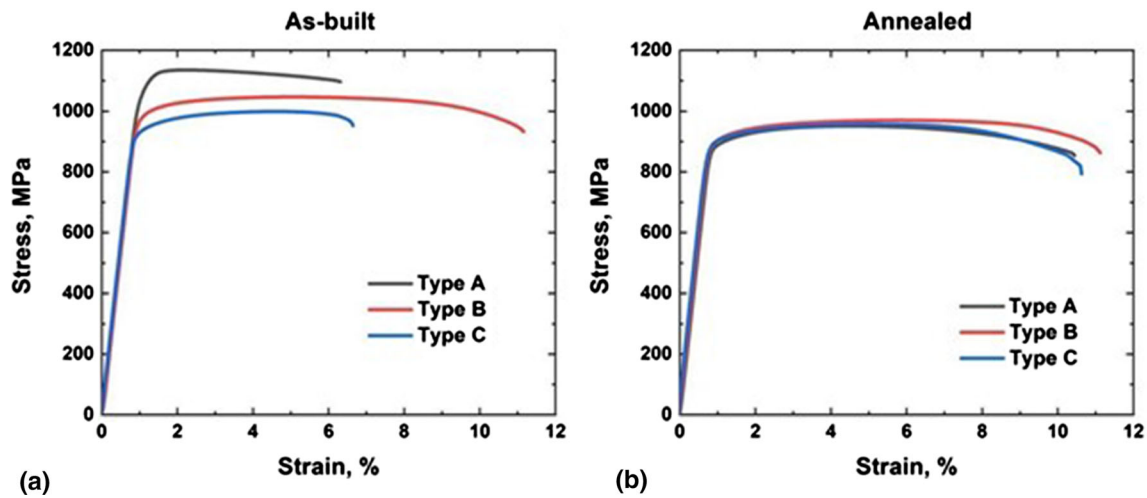


Fig. 9 Typical stress-strain curves of DED Ti-6Al-4V alloy performed with different types of scan strategies (a) before and (b) after annealing at 900 °C for 2 h (Color figure online)

Table 3 Mechanical test results for as-built and heat treated (HT) Ti-6Al-4V samples

	σ_y , MPa	σ_{ult} , MPa	Elongation, %	Microhardness, HV _{0.05}
Type A	1082	1135	5.3	385
Type A+HT	888	951	9.7	347
Type B	983	1047	10.3	347
Type B+HT	899	970	10.4	331
Type C	931	999	5.8	354
Type B+HT	895	958	10.0	341

while for Type B only 5 cycles. These temperature cycles lay in the range of $\alpha \rightarrow \beta$ transformation.

3.2 Mechanical Test Results

Figure 9 consists of the typical stress-strain curves of (a) as-built Ti-6Al-4V samples and (b) annealed at 900 °C samples. It should be noted that all specimens were tensile tested in the X direction according to Fig. 3. The as-built samples of Type A demonstrate comparably the highest strength characteristics of 1082 and 1135 MPa for yield and ultimate strengths, respectively. The lowest strength properties were observed for the samples of Type C, the yield strength is 931 MPa, and the ultimate strength is 999 MPa. The intermediate strength values are achieved by the samples of Type B, 983 and 1047 MPa for the yield and the ultimate strengths, respectively. Type B samples demonstrate the relatively highest elongation value of ~10%, while Type A and C samples show the elongation of ~5%. After annealing at 900 °C, all three types of samples demonstrate similar mechanical behavior, the yield and ultimate characteristics are ~890 and ~960 MPa, respectively, and the elongation is ~10%. Additionally, the annealing is observed to decrease the microhardness for the samples of Type B and C by ~15 HV, while the changes of microhardness for the samples of Type A are ~40 HV. The full mechanical test results are summarized in Table 3.

Figure 10 presents the fracture surfaces of samples printed with three different scan strategy types at (a, c, e) low and (b, d, f) high magnifications. It can be seen that the fracture surface of

Type A sample is characterized by lamellar/cleavage fracture pattern, Fig. 10(b) (dotted lines). Cleavage fracture is a low energy brittle fracture that propagates along low index crystallographic planes (Ref 32). The low magnification of Type B sample fracture surface presents the ductile behavior of the material (Fig. 10c), while the Type C sample demonstrates more brittle fracture character (Fig. 10e). The boundaries of large columnar grains orthogonal to a tensile load can be seen on the fracture surface, Fig. 10(e). At high magnification, the fracture surfaces of Types B and C samples are characterized by transgranular ductile dimple tearing resulting from the coalescence of microvoids, Fig. 10(c) and (f).

4. Discussion

The understanding of structural and phase transformations allows to predict the material properties. As was demonstrated in the present study, the L-DED scan strategies have the essential impact on the material properties due to changes of the structural and phase composition of the Ti-6Al-4V alloy through the thermal history. It should be noted that the task gets more complicated due to cyclic thermal impact on the material.

The possibility of printing the large part is related to increased dwell time between the hatch lines. In the previous work, the significance of dwell time influence between hatch

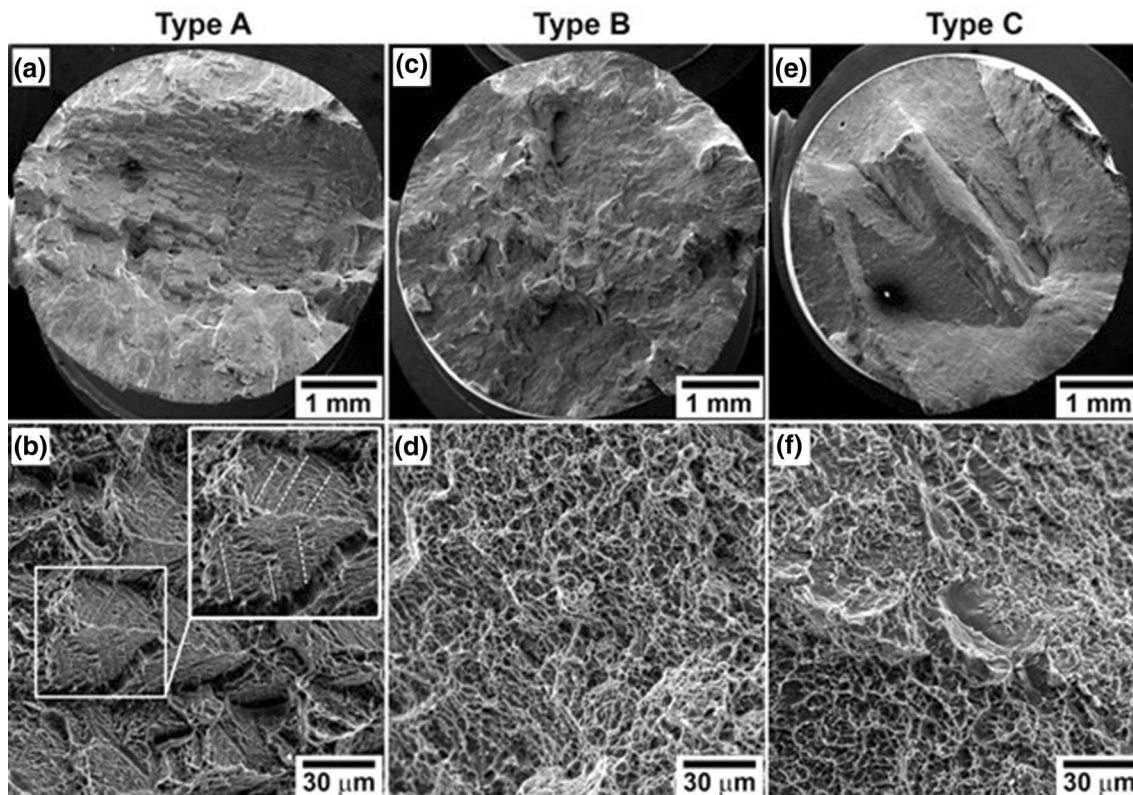


Fig. 10 Fracture surface of as-built DED Ti-6Al-4V tensile samples performed in horizontal direction (X-axis) with (a, b) Type A, (c, d) Type B, and (e, f) Type C scan strategies at low and high magnifications

lines for Type A scan strategy on thermal history and cooling rate of L-DED Ti-6Al-4V alloy using finite element model was shown (Ref 33). Authors demonstrate that the temperature of each material layer cyclically changes in the range of $T_{\min} - T_{\max}$. During the process, the T_{\max} gradually decreases while the T_{\min} stays stable which agrees with the data obtained from the thermocouple in the present study, Fig. 8. Type A samples have the martensite-rich composition and demonstrate relatively low ductility. The highest microhardness of type A sample also proves the highest value of hard and brittle α' phase. The formation of α' phase leading to the crack initiation and part damage during the printing process. The small size of α -lamellae also indicates the high cooling rate of the material. The as-built Type B samples are characterized by the relatively high ductility ($\sim 10\%$) and slightly decreased strength after the post-heat treatment, which can be the result of the residual stress removal. The microhardness did not change significantly after heat treatment which indicates the low contribution of α' phase in strength properties of the as-built sample. The types B and C samples have approximately the same microhardness behavior before and after annealing. However, the martensite-poor Type C samples demonstrate the same ductility as the martensite-rich Type A samples ($\sim 5\%$) with relatively lowest strength properties. The structural characteristics are different for Type B and Type C samples. Type B samples have the equiaxial primary β grains and higher size of α -lamellae having strong texture of $\langle 0001 \rangle$ along the build direction. As well known, the dislocation moves are facilitated at $\{0001\}$ planes. Therefore, such structural features can provide the high ductility. Type C samples have small α -lamellae without preferable orientation. It is possible to conclude that the

specific of Type B structure provides the high mechanical properties for L-DED Ti-6Al-4V alloy. Such structure is formed due to two factors. First, the long heating at elevated temperatures of 550-980 °C forms the bigger α -lamellae. Second, the structural texture of $\langle 0001 \rangle$ along the build direction provides the higher ductility for loads in (0001) plane. However, the further investigations are required to estimate the contribution of each factor to the structural formation.

5. Conclusion

In the present work, the effect of scan strategy on the mechanical and structural properties of L-DED Ti-6Al-4V alloy was investigated. The following statements can be made:

- The long dwell time between the bead lines leads to the formation of hard and brittle α' structure complicating the printing process of massive parts due to crack initiation;
- Continuous hatches provides the heating of the material at temperatures above ~ 550 °C which leads to the decomposition of the martensite phase and formation of dual $\alpha + \beta$ structure;
- Continuous longitudinal hatching forms the texture along the build direction which provides the high ductility of $\sim 10\%$ in transverse direction for the as-built material. Additionally, it presents relatively high strength characteristics of 983 and 1047 MPa for yield and ultimate strengths, respectively.
- After heat treatment, all L-DED Ti-6Al-4V alloy samples

printed with three different strategies demonstrate the same structural and mechanical properties.

Acknowledgments

This research is funded by the Ministry of Science and Higher Education of the Russian Federation as part of the World-class Research Center program: Advanced Digital Technologies (Contract No. 075-15-2020-903 dated 16.11.2020).

References

1. M.J. Donachie, *Titanium: A Technical Guide*, ASM International, 2000
2. C. Veiga, J.P. Davim and A.J.R. Loureiro, Properties and Applications of Titanium Alloys: A Brief Review, *Rev. Adv. Mater. Sci.*, 2012, **32**(2), p 133–148.
3. L.A. Magerramova, G.A. Turichin, Y.A. Nozhnitsky, O.G. Klimova-Korsmik, B.E. Vasiliev, M.E. Volkov and A.V. Salmikov, Peculiarities of Additive Technologies Application in the Production of Gas Turbine Engine Parts, *J. Phys. Conf. Ser.*, 2018, **1109**, p 1. <https://doi.org/10.1088/1742-6596/1109/1/012051>
4. S. Liu and Y.C. Shin, Additive Manufacturing of Ti6Al4V Alloy: A Review, *Mater. Des.*, 2019, **164**, 107552. <https://doi.org/10.1016/j.jm.2018.107552>
5. P. Kümsteiner, M.B. Wilms, A. Weisheit et al., High-Strength Damascus Steel by Additive Manufacturing, *Nature*, 2020, **582**, p 515–519. <https://doi.org/10.1038/s41586-020-2409-3>
6. R. Mendagaliev, O. Klimova-Korsmik, V. Promakhov, N. Schulz, A. Zhukov, V. Klimenko and A. Olisov, Heat Treatment of Corrosion Resistant Steel for Water Propellers Fabricated by Direct Laser Deposition, *Materials*, 2020 <https://doi.org/10.3390/ma13122738>
7. N. Buczak, T. Hassel, N. Kislov, O.G. Klimova-Korsmik, G.A. Turichin and L.A. Magerramova, Phase and Structural Transformations in Heat Resistant Alloys During Direct Laser Deposition, *Key Eng. Mater.*, 2019, **822**, p 389.
8. A.M. Filimonov, O.A. Rogozin, D.G. Firsov, Y.O. Kuzminova, S.N. Sergeev, A.P. Zhilyaev, M.I. Lerner, N.E. Toropkov, A.P. Simonov, I.I. Binkov, I.V. Okulov, I.S. Akhatov and S.A. Evlashin, Hardening of Additive Manufactured 316L Stainless Steel by Using Bimodal Powder Containing Nanoscale Fraction, *Materials*, 2021, **14**, p 115.
9. Y.O. Kuzminova, D.G. Firsov, S.D. Konev, A.A. Dudin, S.A. Dagesyan, I.S. Akhatov and S.A. Evlashin, Structure Control of 316L Stainless Steel Through an Additive Manufacturing, *Lett. Mater.*, 2019, **9**(4s), p 551–555.
10. J. Karimi, C. Suryanarayana, I. Okulov and K.G. Prashanth, Selective Laser Melting of Ti6Al4V: Effect of Laser Re-melting, *Mater. Sci. Eng. A.*, 2021, **805**, 140558. <https://doi.org/10.1016/j.msea.2020.140558>
11. L. Xi, K. Ding, D. Gu, S. Guo, M. Cao, J. Zhuang, K. Lin, I. Okulov, B. Sarac, J. Eckert and K.G. Prashanth, Interfacial Structure and Wear Properties of Selective Laser Melted Ti(TiC+TiN) Composites with High Content of Reinforcements, *J. Alloys Compd.*, 2021, **870**, 159436. <https://doi.org/10.1016/j.jallcom.2021.159436>
12. J. Alcisto, A. Enriquez, H. Garcia et al., Tensile Properties and Microstructures of Laser-Formed Ti-6Al-4V, *J. Mater. Eng. Perform.*, 2011, **20**, p 203–212. <https://doi.org/10.1007/s11665-010-9670-9>
13. B. Wysocki, P. Maj, R. Sitek, J. Buhagiar, K.J. Kurzydłowski and W. Świąszkowski, Laser and Electron Beam Additive Manufacturing Methods of Fabricating Titanium Bone Implants, *Appl. Sci.*, 2017, **7**, p 657.
14. E. Dolgun, E. Zemlyakov, S. Shalnova, M. Gushchina and V. Promahov, The Influence of Heat Treatment on the Microstructure of Products Manufactured by Direct Laser Deposition Using Titanium Alloy Ti-6Al-4V, *Mater. Today Proc.*, 2020, **30**, p 688–693. <https://doi.org/10.1016/j.matpr.2020.01.523>
15. J. Yu, M. Rombouts, G. Maes and F. Motmans, Material Properties of Ti6Al4V Parts Produced by Laser Metal Deposition, *Phys. Procedia*, 2012, **39**, p 416–424. <https://doi.org/10.1016/j.phpro.2012.10.056>
16. I. Yadroitsev, P. Krakhmalev and I. Yadroitsava, Selective Laser Melting of Ti6Al4V Alloy for Biomedical Applications: Temperature Monitoring and Microstructural Evolution, *J. Alloys Compd.*, 2014, **583**, p 404–409. <https://doi.org/10.1016/j.jallcom.2013.08.183>
17. L. Qian, J. Mei, J. Liang and X. Wu, Influence of Position and Laser Power on Thermal History and Microstructure of Direct Laser Fabricated Ti-6Al-4V Samples, *Mater. Sci. Technol.*, 2005, **21**(5), p 597–605. <https://doi.org/10.1179/174328405X21003>
18. S.A. Shalnova, G.A. Panova and N. Buczak, Structure and Phase Composition of Ti-6Al-4V Samples Produced by Direct Laser Deposition, *Key Eng. Mater.*, 2019, **822**, p 467–472.
19. T. Ahmed and H.J. Rack, Phase Transformations During Cooling in $\alpha + \beta$ Titanium Alloys, *Mater. Sci. Eng. A*, 1998, **243**, p 206–211.
20. H. Galarraga, R.J. Warren, D.A. Ladoss, R.R. Dehoff, M.M. Kirka and P. Nandwana, Effects of Heat Treatments on Microstructure and Properties of Ti-6Al-4V ELI Alloy Fabricated by Electron Beam Melting (EBM), *Mater. Sci. Eng. A.*, 2017, **685**, p 417–428. <https://doi.org/10.1016/j.msea.2017.01.019>
21. M. Simonelli, Y. Tse and C. Tuck, The Formation of $\alpha \beta$ Microstructure in As-Fabricated Selective Laser Melting of Ti-6Al-4V, *J. Mater. Res.*, 2014, **29**(17), p 2028–2035. <https://doi.org/10.1557/jmr.2014.166>
22. H. Jia, H. Sun, H. Wang et al., Scanning Strategy in Selective Laser Melting (SLM): A Review, *Int. J. Adv. Manuf. Technol.*, 2021, **113**, p 2413–2435. <https://doi.org/10.1007/s00170-021-06810-3>
23. K. Prasad, M. Obana, Y. Ishii, A. Ito and S. Torizuka, The Effect of Laser Scanning Strategies on the Microstructure, Texture and Crystallography of Grains Exhibiting Hot Cracks in Additively Manufactured, *Hastelloy X Mech. Mater.*, 2021, **157**, p 103816.
24. M. Strantza, R.K. Ganeriwala, B. Clausen, T.Q. Phan, L.E. Levine, D.C. Pagan, J.P.C. Ruff, W.E. King, N.S. Johnson, R.M. Martinez, V. Anghel, G. Rafailov and D.W. Brown, Effect of the Scanning Strategy on the Formation of Residual Stresses in Additively Manufactured Ti-6Al-4V, *Addit. Manuf.*, 2021, **45**, 102003. <https://doi.org/10.1016/j.addma.2021.102003>
25. P.L. Stephenson, N. Haghdad, R. DeMott, X.Z. Liao, S.P. Ringer and S. Primg, Effect of Scanning Strategy on Variant Selection in Additively Manufactured Ti-6Al-4V, *Addit. Manuf.*, 2020, **36**, 101581. <https://doi.org/10.1016/j.addma.2020.101581>
26. T. Petrat, R. Winterkorn, B. Graf et al., Build-up Strategies for Temperature Control Using Laser Metal Deposition for Additive Manufacturing, *Weld World*, 2018, **62**, p 1073–1081. <https://doi.org/10.1007/s40194-018-0604-8>
27. Y. Lee, Y. Bandari, P. Nandwana, B.T. Gibson, B. Richardson and S. Simunovic, Effect of Intercooling Time, Constraints and Tool Path Strategy on Deformation of Large Laser-Welded Components, *Appl. Sci.*, 2019, **9**(23), p 5115. <https://doi.org/10.3390/app9235115>
28. R., Hama-Saleh, K. Yildirim, S., Hemes, A., Weisheit, & C. Häfner, Investigation of High-Deposition-Rate Additive Manufacturing of Ti-6Al-4V via Laser Material Deposition. Paper presented at ESAFORM 2021. 24th International Conference on Material Forming, Liège, Belgique (2021). <https://doi.org/10.25518/esaform21.486>
29. T. DebRoy, H.L. Wei, J.S. Zuback, T. Mukherjee, J.W. Elmer, J.O. Milewski, A.M. Beese, A. Wilson-Heid, A. De and W. Zhang, Additive Manufacturing of Metallic Components: Process, Structure and Properties, *Prog. Mater. Sci.*, 2018, **92**, p 112–224. <https://doi.org/10.1016/j.pmatsci.2017.10.001>
30. G. Luetjering and J.C. Williams, *Titanium*, 2nd ed. Springer, New York, 2007. <https://doi.org/10.1007/978-3-540-73036-1>
31. J. Han, J. Yang, H. Yu, J. Yin, M. Gao, Z. Wang and X. Zeng, Microstructure and Mechanical Property of Selective Laser Melted Ti6Al4V Dependence on Laser Energy Density, *Rapid Prototyp. J.*, 2017, **23**(2), p 217–226. <https://doi.org/10.1108/RPJ-12-2015-0193>
32. G.E. Dieter, *Mechanical Metallurgy*, McGraw Hill, New York, 1986
33. M.O. Gushchina, S.Y. Ivanov and A.M. Vildanov, Effect of Temperature Field on Mechanical Properties of Direct Laser Deposited Ti-6Al-4V Alloy, *Conf. Ser. Mater. Sci. Eng.*, 2020, **969**, p 12103. <https://doi.org/10.1088/1757-899x/969/1/012103>

Publisher's Note Springer Nature remains neutral with regard to jurisdictional claims in published maps and institutional affiliations.